NASA Technical Memorandum 81264

USAAVRADCOM TR 81-A-6

The Phenomenon of Dynamic Stall

W. J. McCroskey

March 1981

NASA

NASA Technical Memorandum 81264 USAAVRADCOM TR 81-A-6

The Phenomenon of Dynamic Stall

W. J. McCroskey, Aeromechanics Laboratory
AVRADCOM Research and Technology Laboratories
Ames Research Center, Moffett Field, California

Ames Research Center

Lecture Notes On

THE PHENOMENON OF DYNAMIC STALL

by

W. J. McCroskey

Ames Research Center, NASA
and
U. S. Army Research and Technology Laboratories (AVRADCOM)
Ames Research Center
Moffett Field, California, USA

Presented to von Kármán Institute Lecture Series on

Unsteady Airloads and Aeroelastic Problems in Separated

and Transonic Flows

Rhode-Saint-Genèse, Belgium
9-13 March 1981

THE PHENOMENON OF DYNAMIC STALL

W. J. McCroskey

Ames Research Center, NASA and U. S. Army Research
and Technology Laboratories (AVRADCOM)
Ames Research Center, Moffett Field, California, USA

1. INTRODUCTION

Stall and its consequences are fundamentally important to the design and operation of flight vehicles. A certain degree of unsteadiness always accompanies the flow over an airfoil or other streamlined body at high angle of attack, but the stall of a lifting surface undergoing unsteady motion is even more complex than static stall. Although much progress has been made in recent years, dynamic stall remains a major unsolved problem with a variety of current applications in aeronautics, hydrodynamics, and wind engineering.

These lectures will summarize the main physical features of the phenomenon and the attempts that have been made to predict it. The information presented is drawn mainly from recent review articles (Ref. 1-5) and investigations by the author and his colleagues (Refs. 6-9). Since a large fraction of the existing knowledge has come from experimental research, the details of dynamic stall are discussed principally in physical terms.

2. GENERAL FEATURES

Above a certain critical angle of attack, the flow around a slender lifting surface breaks down into the phenomenon called stall. On an oscillating airfoil whose incidence is increasing rapidly, the onset of the stall can be delayed to incidences considerably in excess of the static stall angle. Once dynamic stall does occur, however, it is usually more severe and more persistent than static stall. The attendant aerodynamic forces and moments exhibit large amounts of hysteresis with respect to the instantaneous angle of attack $\alpha(t)$, especially if α oscillates around some mean value α_o that is of the order of the static stall angle α_{ss}.

2.1 Dynamic Stall Events

Numerous experiments have shown that dynamic stall is characterized by the shedding and passage over the upper surface of the lifting surface of a vortex-like disturbance. This viscous disturbance induces a highly nonlinear, fluctuating pressure field (illustrated in Fig. 1). If the frequency, amplitude, and maximum incidence are sufficiently high, the vortex-shedding phenomenon is well organized and clearly defined.

It begins near the leading edge and passes through the distinct stages illustrated in Figs. 2 and 3. Figure 2 and the accompanying Table 1 show the typical hysteresis in C_L, C_M, and C_D versus angle of attack, while Fig. 3 indicates the loci of the various stall events on the airfoil plotted in an x-t diagram.

In the unseparated region between points 1 and 2 in Figs. 2 and 3, the lift and pitching moment follow approximately the trends of unsteady linear thin airfoil theory. Sometime after α exceeds α_{ss}, a thin layer of reversed flow develops at the bottom of the boundary layer. On the so-called trailing-edge stalling airfoils (e.g., Fig. 3), this tongue of reversed flow starts at the rear of the airfoil and moves forward to the leading-edge region, whereas on leading-edge stalling profiles it develops

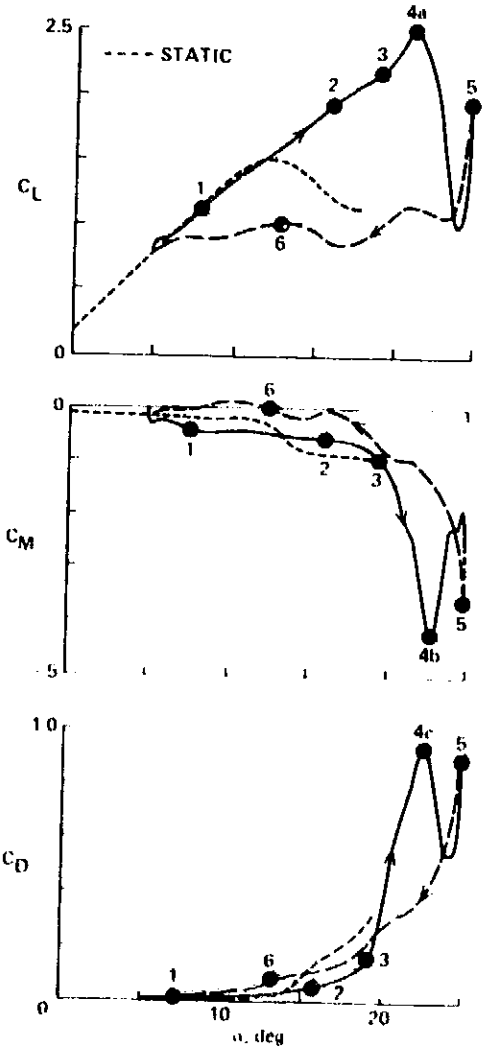

Fig. 2. Dynamic stall events on the Vertol VR-7 airfoil at $M_\infty = 0.25$, $\alpha = 15° + 10° \sin \omega t$, and $k = 0.10$. Points defined in Table 1.

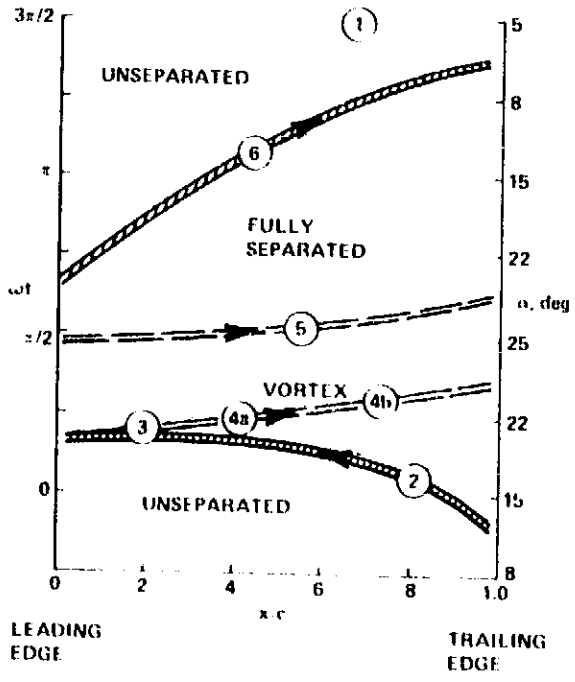

Fig. 3. Loci of dynamic stall events over the upper surface of the oscillating airfoil of Fig. 2. Points 1–6 defined in Table 1.

TABLE 1.- THE DYNAMIC STALL EVENTS OF FIGS. 2 AND 3

Point	Flow structure	Forces and moments
1	Thin attached boundary layer	Linear regime
2	Flow reversals within boundary layer	Exceed static $C_{L_{max}}$, extrapolate linear regime
3	Vortex detaches and moves over airfoil surface	Pitching moment diverges, vortex lift present
4	Vortex continues toward trailing edge	Maximum lift and moment, followed by rapid decay
5	Secondary vortex	Secondary peaks
6	Reattachment of flow from leading edge	Readjust to linear regime

quickly and very locally just downstream of the suction peak on the upper surface. In either case, a vortex then begins to evolve near the leading-edge region and spread rearward, as shown in the two center scenes in Fig. 1, at a speed somewhat less than $1/2U_\infty$. The associated distortion in the pressure distribution causes the quarter-chord pitching moment to diverge from its previous trend, at point 3 in Figs. 2 and 3, to large negative values. The drag also begins to rise dramatically. However, unlike static stall, the lift usually continues to increase monotonically until the vortex is well past midchord.

As the vortex nears the trailing edge, lift, moment, and drag reach their largest values (point 4), although usually not exactly simultaneously, and then drop dramatically. Secondary and sometimes tertiary vortices produce additional fluctuation in the airloads, point 5, but at greatly reduced levels. If α is decreasing in the meantime, the flow will begin to reattach, point 6, at some angle of attack much less than α_{ss}. The reattachment point moves rearward at a speed well below U_∞ so that several chord lengths of travel are required before the flow completely returns to the approximately linear domain.

The dynamic airloads are, of course, manifestations of the unsteady pressure distributions on the airfoil. Therefore, it is instructive to look at C_p as a function of space and time. Figure 4 shows the pressure distribution at discrete times, obtained from 16 miniature pressure transducers distributed over the upper surface of the airfoil. Figure 5 shows the continuous time histories of each of these 16 transducers. The abrupt collapse of suction around the leading edge and passage of the primary and secondary vortices are particularly evident in these figures.

2.2 Hysteresis and Aerodynamic Damping

Each of the aforementioned dynamic stall events takes a finite amount of time to develop, scaling approximately as $U_\infty \Delta t/c$. However, once they are initiated, they tend to be relatively independent of the airfoil motion. In addition to the obvious implications for mathematical modeling of the phenomenon, this has two important physical consequences. The first is the lag and asymmetry of the airloads with respect to the motion of the body; this produces the hysteresis discussed in Section 2.1 and readily apparent in Fig. 2. This represents an important contrast to the quasi-steady limit, for which the flow field adjusts immediately to each change in incidence. In the steady

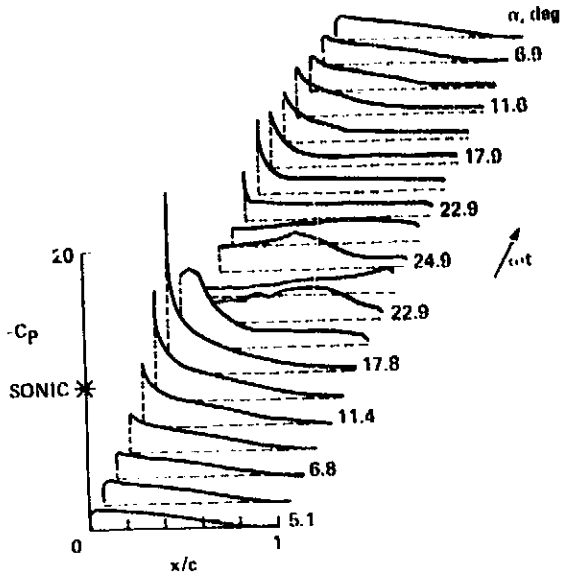

Fig. 4. Pressure distributions at various times during dynamic stall for the conditions of Fig. 2.

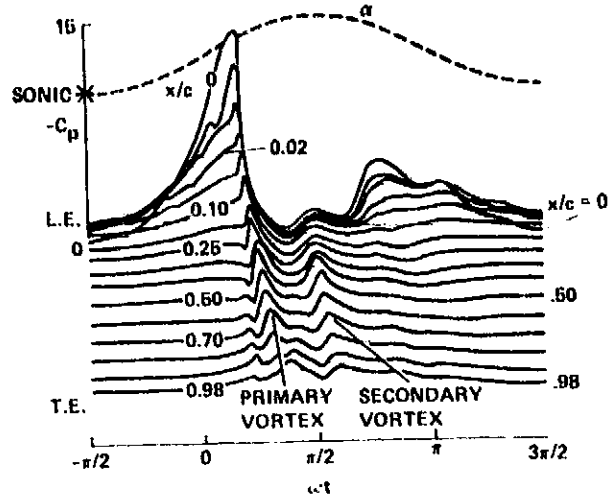

Fig. 5. Time histories of pressures at various points on the airfoil of Fig. 2.

case, the aerodynamic forces are approximately unique functions of α, whether α is increasing or decreasing; therefore, angle of attack becomes a primary parameter to the aerodynamicist. It remains an important one in unsteady separated flow, but it is clearly not so unique.

The second and closely related point concerns what the aerodynamicist considers to be aerodynamic damping or, more properly, the net aerodynamic work per cycle of oscillation, and its relationship to flutter. For a pitching airfoil, the instantaneous work done on the fluid by the body due to its motion is $dW = -Md\alpha$, where M is the pitching moment about the axis of rotation and is positive for nose-down airloads. Although the product of $C_M d\alpha$ is normally negative, during some phases of dynamic stall it can become positive, so the fluid is doing work on the body instead of vice versa.

The so-called pitch-damping parameter, given by $\zeta = -\oint C_M d\alpha / 4\alpha_1^2$, is a measure of the net work done over a complete cycle of oscillation. If ζ is negative, the airfoil extracts energy from the airstream, and the pitch oscillations will tend to increase in amplitude unless restrained. This, of course, is the condition for flutter, and the hysteresis of dynamic stall permits it to occur in a single degree of freedom of oscillatory body motion. Normally, in unseparated flows flutter only occurs when the body motion includes multiple degrees of freedom, e.g., combined bending and torsion of an aircraft wing.

Stall flutter, arising from this negative pitch damping, tends to occur when the airfoil is oscillating in and out of stall. As indicated in Fig. 6 from Ref. 10, the damping is given by the area inside the $C_M - \alpha$ trace. For this example, it is positive throughout the cycle when $\alpha_0 = 7.3°$, i.e., when no stall occurs, and when $\alpha_0 = 24.6°$, i.e., when the airfoil remains stalled throughout the cycle. However, for $\alpha_0 = 14.9°$, the airfoil is stalled part of the time and not at other times, and the areas inside the clockwise loops ($\zeta < 0$) and counterclockwise loops ($\zeta > 0$) are approximately the same. This indicates neutral stability. Had the mean angle been slightly less, the net damping would probably have been negative and the oscillation would therefore have been unstable if unrestrained.

Stall-induced negative damping can occur in other types of motion, such as plunging oscillations (Ref. 10). In this case, the aerodynamic work is $dW = Ldh$, where h is the displacement of the airfoil perpendicular to the oncoming flow. As before, unstalled motion is normally stable, and the tendency toward instability is greatest when the airfoil oscillates in and out of stall.

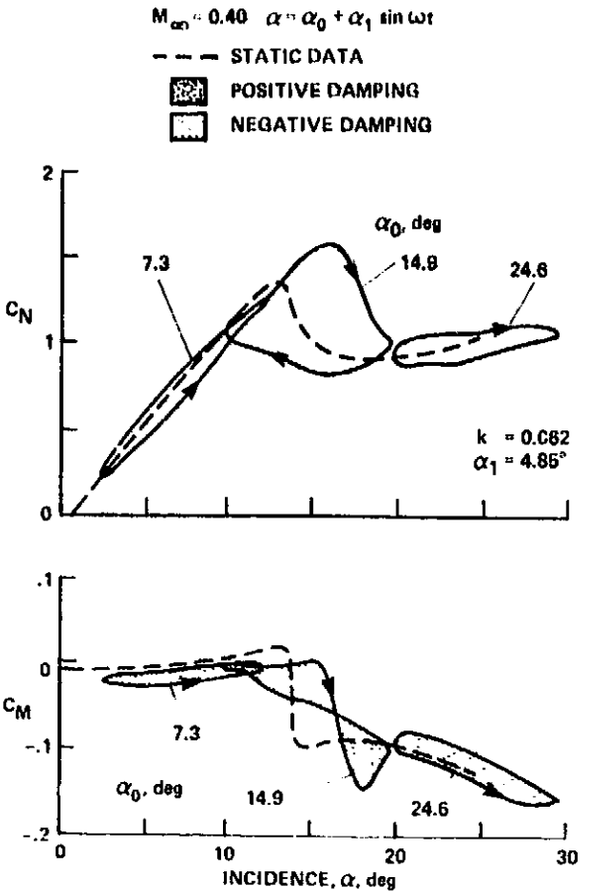

Fig. 6. The effect of mean angle on lift and moment coefficients and on aerodynamic damping.

3. STALL REGIMES

The flow field around an oscillating airfoil in subsonic flow can be characterized by the degree or extent of flow separation. For a given airfoil, the primary parameter that determines the degree of separation is the maximum angle of attack ($\alpha_{max} = \alpha_0 + \alpha_1$ for sinusoidal oscillations). An important aspect of dynamic stall is the large amplitudes of the motion which produce the large maximum angles. This contrasts with the hierarchy of viscous effects on oscillating airfoils at transonic speeds and low angles of attack, where the scale of the interaction is governed primarily by the strength and motion of the shock wave. So far, prediction methods for this class of problems have not been successful for the low-speed, high-angle problems and vice versa.

The importance of α_{max} is illustrated in Fig. 7 (from Ref. 8), which portrays four important regimes of viscous-inviscid interaction for oscillating airfoils. For the left-hand part of the figure, i.e., $\alpha_{max} = 13°$, there is almost no separation throughout the cycle, although unsteady boundary-layer displacement thickness effects are not completely negligible. When α_{max} is increased to 14°, the limited separation that occurs during a small fraction of the cycle distorts the hysteresis loops of the unsteady pressures and airloads. From a practical standpoint, the effect on C_M is particularly important. This stall-onset condition represents the limiting case of the maximum lift that can be obtained with no significant penalty in pitching moment or drag.

A slight additional increase in α_{max} to 15° produces a major increase in the extent, severity, and duration of the separation phenomenon, for the conditions shown in Fig. 7. This type of viscous-inviscid interaction produces what is called "light dynamic stall" (Refs. 8-9). Further increases in α_{max} lead to the deep dynamic stall regime, with a large viscous zone over the entire upper surface of the airfoil during half or more of the cycle.

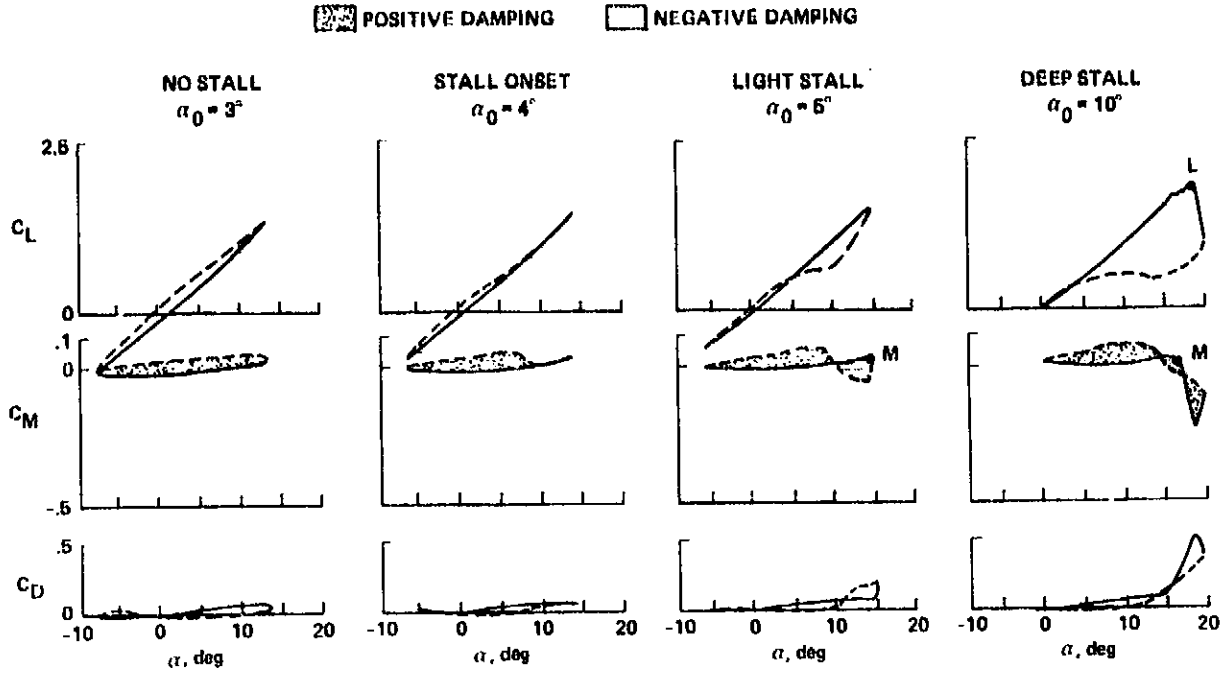

Fig. 7. Dynamic stall regimes. NACA 0012 airfoil, $\alpha = \alpha_o + 10° \sin \omega t$, $k = 0.10$; solid lines denote increasing α, dashed lines decreasing α.

3.1 Light Stall

This category of dynamic stall shares some of the general features of classical static stall, such as loss of lift and significant increases in drag and nose-down pitching moment compared to the theoretical inviscid values, when α exceeds a certain value. In addition, the unsteady stall behavior is characterized by large phase lags and hystereses in the separation and reattachment of the viscous flow and, consequently, in the airloads. Also, the tendency toward negative aerodynamic damping, as discussed above, is strongest in this regime.

Another distinguishing feature of the light dynamic stall is the scale of the interaction. The vertical extent of the viscous zone tends to remain on the order of the airfoil thickness, generally less than for static stall. Consequently, this class of oscillating airfoil problems should be within the scope of zonal methods or thin-layer Navier-Stokes calculations with relatively straightforward turbulence modeling.

The quantitative behavior of light stall is known to be especially sensitive to airfoil geometry, reduced frequency, maximum incidence, and Mach number; also, three-dimensional effects and the type of motion are probably important. The qualitative behavior is closely related to the boundary-layer-separation characteristics, e.g., leading-edge versus trailing-edge separation, and to the changes in this separation behavior with α_{max}, k, and M_∞. The effects of these parameters are discussed in Section 4.

3.2 Deep Stall

The vortex-shedding phenomenon discussed previously is the predominant characteristic of this dynamic stall regime. The passage of the vortex over the upper surface of the airfoil produces values of C_L, C_M, and C_D far in excess of their static counterparts when α is increasing, and large amounts

of hysteresis occur during the rest of the cycle. The scale of the viscous interaction zone is also large; the thickness of the viscous layer is on the order of the airfoil chord during the vortex-shedding process.

Figures 7 and 8 (from Ref. 8) illustrate some of the qualitative and quantitative differences in light and deep dynamic stall. Moment stall, denoted by M, occurs rather abruptly for all three values of α_0, but the deep stall drop in lift after C_{Lmax}, denoted by L, is not evident in the light stall case. The large negative values of C_M are due to the vortex.

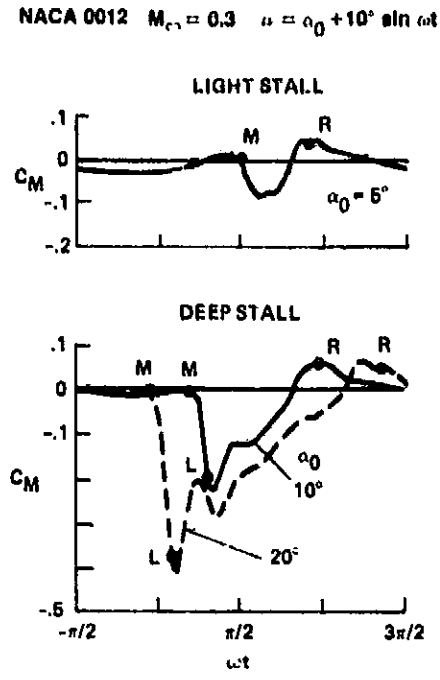

Fig. 8. Effect of mean angle on the time history of pitching moment coefficient for the conditions of Fig. 7.

The qualitative features of deep stall are less sensitive to the details of the airfoil motion, airfoil geometry, Reynolds number, and Mach number, provided strong shock waves do not develop (Ref. 8). The quantitative airloads depend primarily on the time history of the angle of attack for the portion of the cycle when α exceeds the static stall angle α_{ss}. This feature and other details of the flow behavior will become evident in the following discussions.

4. EFFECTS OF VARIOUS PARAMETERS

One of the reasons that dynamic stall is more difficult to analyze and predict than static stall is its dependence on a much larger number of parameters. Table 2 gives a general indication of some of the more important ones and their effects.

4.1 Airfoil Geometry

Especially in the light stall regime, the leading-edge geometry of an airfoil is a principal factor in determining the boundary-layer separation characteristics. Airfoils with moderately sharp leading edges tend to develop severe adverse pressure gradients in the first few percent of chord, leading to abrupt boundary-layer separation there that spreads rapidly downstream. This is referred to as "leading-edge stall," and it produces a relatively concentrated vortex and abrupt changes in C_L, C_M, and C_D during the development of the dynamic stall events. This contrasts with trailing-edge stall, which is more common on airfoils with relatively blunt noses or large amounts of leading-edge camber. In this case, the boundary-layer separation progresses forward from the trailing edge, the onset of stall tends to occur more gradually, and unsteady effects tend to suppress the separation more than on leading-edge stalling airfoils. Also, the more gradual the trailing-edge separation, the less likely negative aerodynamic damping will occur.

Figures 9 and 10 show some of the airfoil sections that have been studied by the author and his colleagues (Refs. 6-8). Results in the light

TABLE 2.- IMPORTANCE OF DYNAMIC STALL PARAMETERS

Stall parameter	Effect
Airfoil shape	Large in some cases
Mach number	Small below $M_\infty \sim 0.2$, Large above $M_\infty \sim 0.2$
Reynolds number	Small (?) at low Mach number, Unknown at high Mach number
Reduced frequency	Large
Mean angle, amplitude	Large
Type of motion	Virtually unknown
Three-dimensional effects	Virtually unknown
Tunnel effects	Virtually unknown

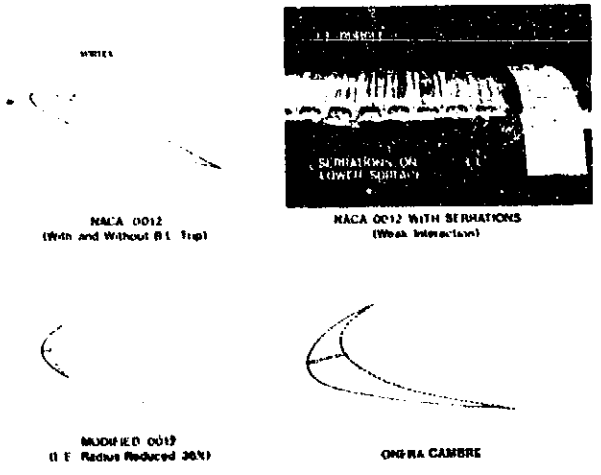

Fig. 9. Leading-edge geometries studied in Refs. 6 and 7.

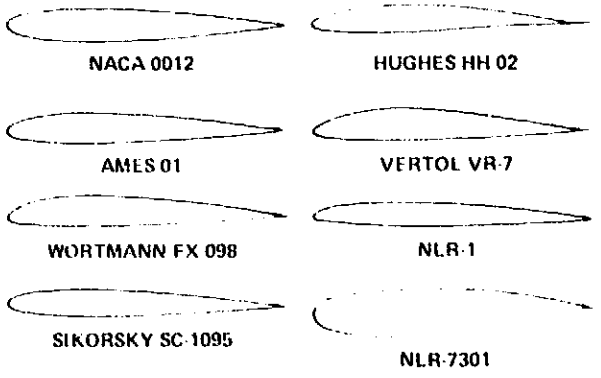

Fig. 10. Airfoils studied in Ref. 8.

stall and stall onset regimes for the profiles in Fig. 10 are shown in Fig. 11, which illustrates how widely the aerodynamic coefficients can vary for one set of unsteady conditions.

The type of boundary-layer separation is listed for each section in Fig. 11. In this example, the maximum incidence, 15°, was more than 1° greater than the static stall angle of all the airfoils, except the NLR-7301. Consequently, the other seven sections exhibited some dynamic overshoot of $C_{l_{max}}$. However, this came at the expense of large pitching moments on the NACA 0012, Wortmann FX-098, Sikorsky SC-1095, Hughes HH-02, and NLR-1 airfoils, and negative pitch damping on the 0012 and SC-1095.

The differences between these airfoils are diminished in deep stall, where the vortex shedding becomes fully developed. Figure 12 (from Ref. 8) shows the lift, moment, and drag results for four of the eight sections in Figs. 10 and 11. The hysteresis loops for the Ames-01, VR-7, and NLR-1 airfoils are remarkably similar, differing principally in the angle for the

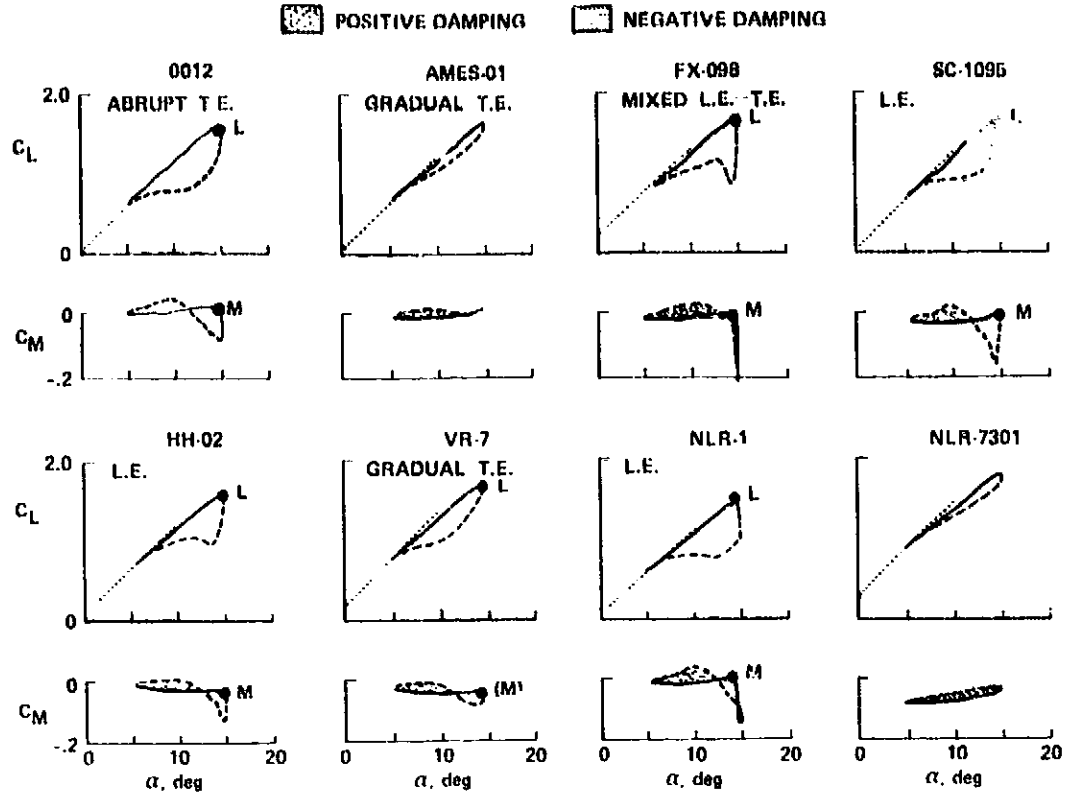

Fig. 11. Light-stall airloads at $M_\infty = 0.30$, $\alpha = 10° + 5° \sin \omega t$, and $k = 0.10$. Solid lines denote increasing α, dashed lines decreasing α, dotted lines static data.

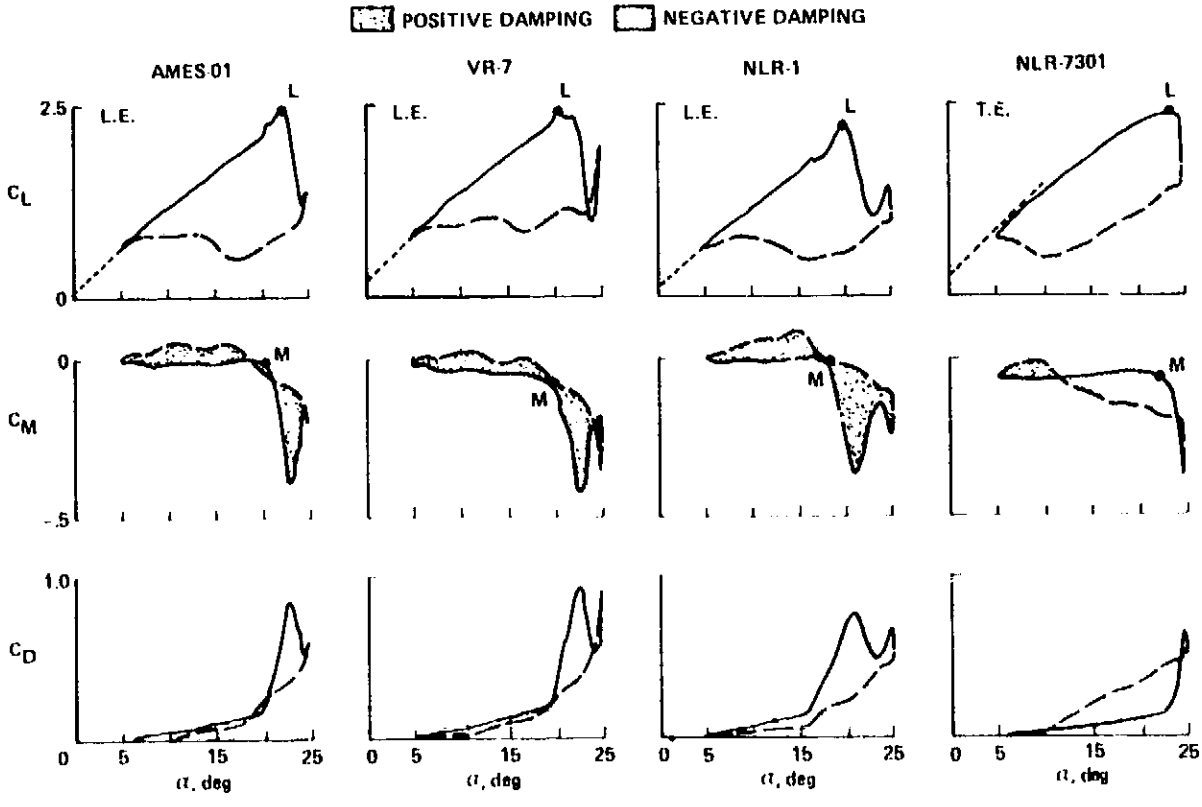

Fig. 12. Deep-stall airloads at $M_\infty = 0.26$, $\alpha = 15° + 10° \sin \omega t$, and $k = 0.10$.

onset of stall, in the magnitude of the peak forces and moments, and in the strength of the secondary vortex at or near α_{max}. The same could be said for the other four airfoils (not shown).

4.2 Reduced Frequency

An important parameter affecting dynamic stall is obviously the reduced frequency of the oscillation, but its influence depends on the stall regime and the type of boundary-layer separation. For example, Figs. 13 and 14 (from Ref. 9) show opposite trends in the light stall regime for leading-edge and trailing edge stalling airfoils tested under identical conditions. On the other hand, Fig. 15 (from Ref. 2) is more representative of the trends in deep dynamic stall. In this case, the vortex-shedding phenomenon developed for

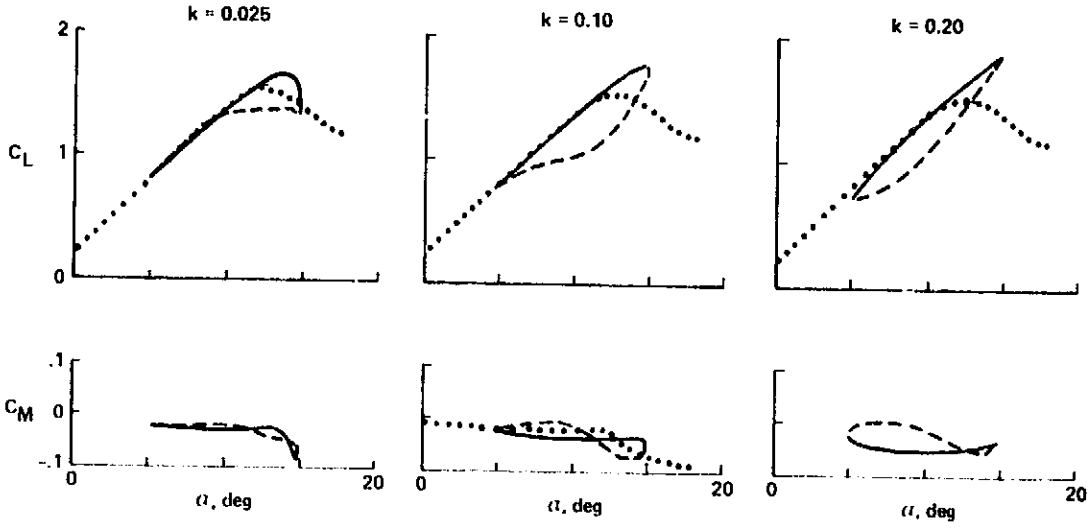

Fig. 13. The effect of reduced frequency on the VR-7 airfoil at $M_\infty = 0.30$ *and* $\alpha = 10° + 5° \sin \omega t$.

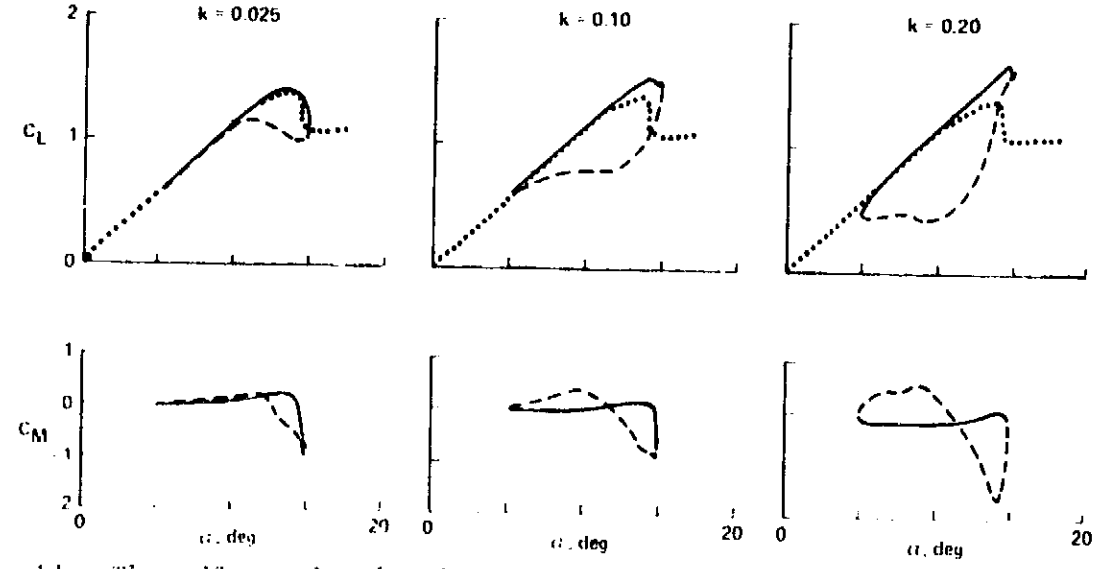

Fig. 14. The effect of reduced frequency on the NACA 0012 airfoil at $M_\infty = 0.60$ *and* $\alpha = 10° + 5° \sin \omega t$.

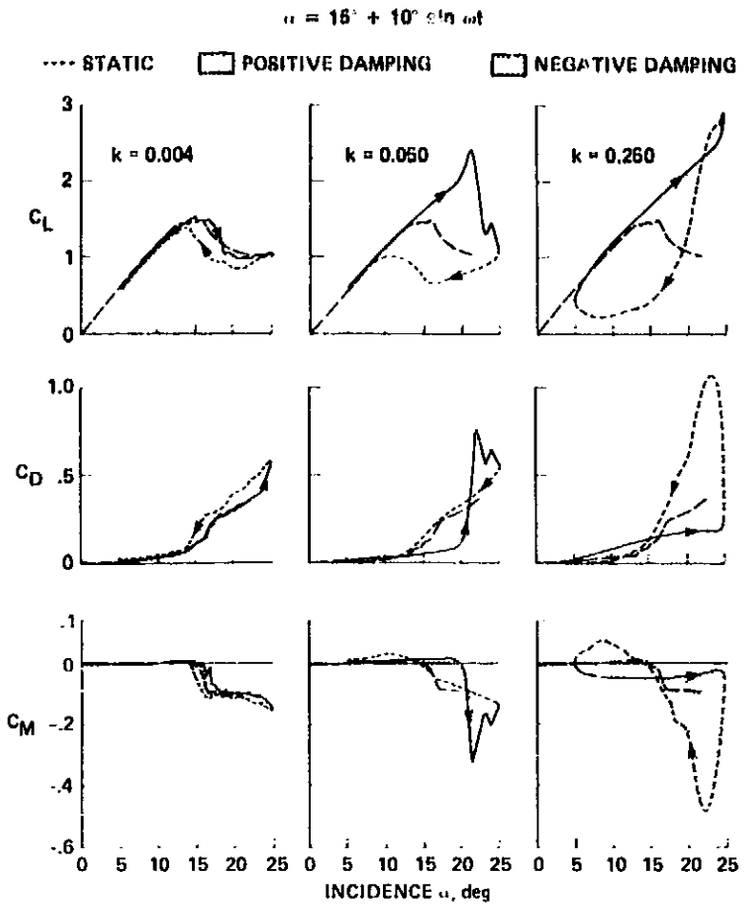

Fig. 15. The effect of reduced frequency in the deep stall regime. NACA 0012, $M_\infty = 0.10$.

$k \geq 0.05$ and the strength of the vortex appeared to become independent of reduced frequency for $k \geq 0.15$.

4.3 Amplitude and Mean Angle

For periodic motion, α_0 and α_1 cannot be completely separated since $\alpha_{max} = \alpha_0 + \alpha_1$ is very important in determining the amount of separation. This was discussed previously in connection with Figs. 6 to 8; but in those examples, α_1 remained constant while α_0 varied. On the other hand, Fig. 16 shows the effect of varying α_1 with α_0 and the pitch rate parameter $\dot{\alpha}_{max}$ held constant ($\dot{\alpha}_{max}c/U_\infty = 2\alpha_1 k$). For the deep stall cases of $\alpha_1 = 10°$ and 14°, the vortex-shedding phenomenon begins while α is still increasing. The subsequent flow-field development is very similar for these two cases, although the different stall events occur at different phases in the cycle. However, when $\alpha_1 = 6°$, dynamic stall does not begin until after α_{max}; this occurs as α is decreasing. As a result, the vortex effect is less pronounced, and the results are more representative of light stall. This is not unexpected and, in the limit of very small amplitude, the vortex would essentially disappear.

An interesting comparison can be made if combinations of α_0, α_1, and k are selected to match the $\alpha(t)$ histories over the portion of the cycle where α exceeds the static stall angle. One such example is shown in Fig. 17. In these two data sets, the pitch rates, $\dot{\alpha}$, are very nearly the same at $\alpha = 17°$, which is about where moment stall begins. The lift and moment data

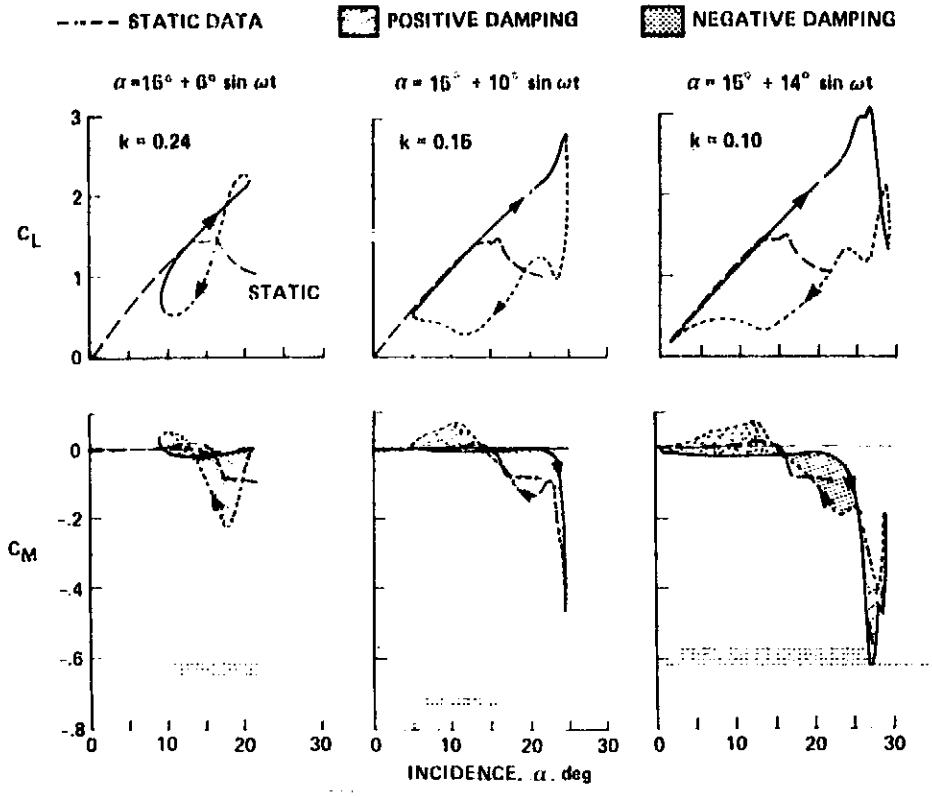

Fig. 16. The effect of amplitude at $\dot{\alpha}_{max}\, c/U_\infty \cong 0.05$.

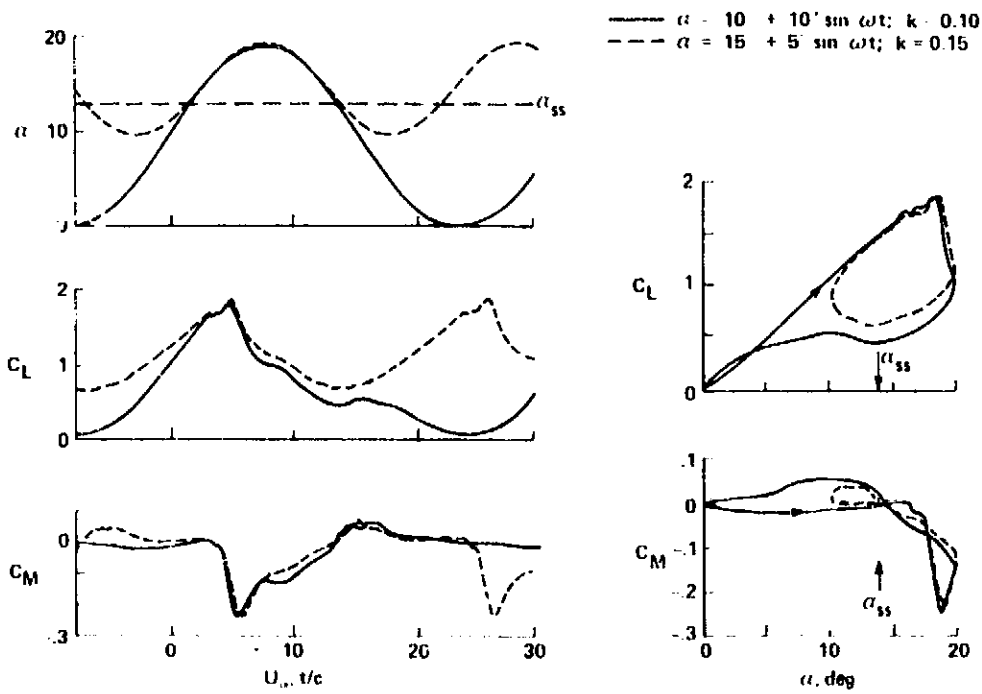

Fig. 17. Dynamic airloads for $\alpha_{max} = 30°$ *and* $\alpha_1 k^2 \cong 0.002$.

are almost identical on the upstroke and throughout most of the stall events, whether viewed versus $U_\infty t/c$ or versus α. This would not be the case if the $\alpha(t)$ histories were not so closely matched.

A close examination of numerous cases from Ref. 8 and elsewhere indicates the general rule that the better the match between the $\alpha(t)$ histories between

$\alpha_{static\ stall}$, α_{max}, and $\alpha_{reattachment}$, the better the match between the aerodynamic coefficients, at least for pitching motions in deep stall. However, the extent to which this conclusion can be extended to light stall or to other types of motion remains to be established.

4.4 Mach Number

Even at relatively low free-stream Mach number, supersonic flow can develop near the leading edge of an airfoil at high incidence. This is shown schematically in Fig. 18, in comparison with the more conventional transonic airfoil problem. As M_∞ increases, eventually the supersonic zone would be expected to terminate in a shock wave of sufficient strength to cause boundary-layer separation and leading-edge stall. The impact of such shock-induced separation on dynamic stall in general, and on the vortex-shedding phenomenon in particular, has not yet been assessed to any significant extent.

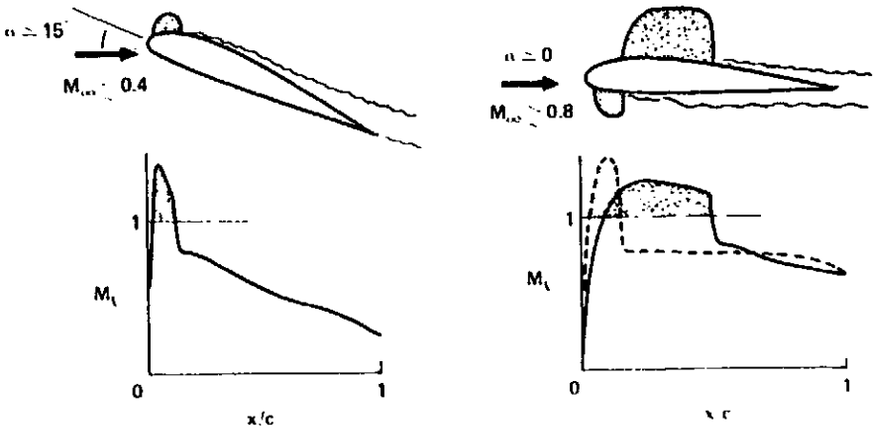

Fig. 18. Sketch of two types of transonic flow on airfoils.

Figure 19 shows some effects of increasing Mach number on dynamic stall. The data are taken from Liiva et al. (Ref. 10); here progressively smaller mean angles were selected because of the decrease in the static stall angle with increasing Mach number. The similarity of the static stall characteristics at M = 0.2 and 0.4 suggests that transonic shock-wave formation does

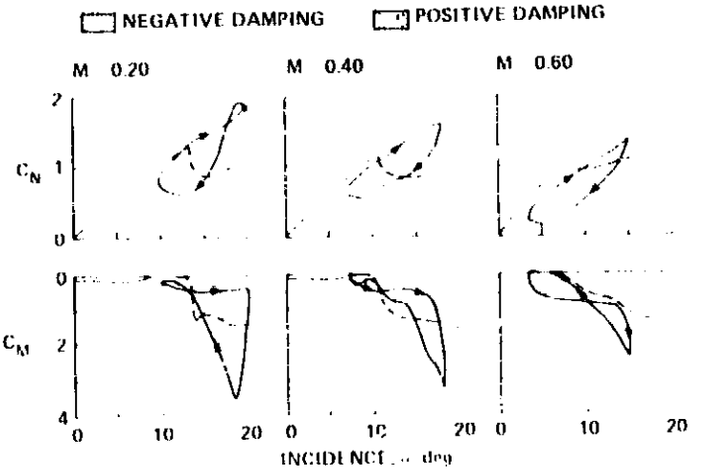

Fig. 19. Effects of Mach number on dynamic force and moment coefficients.

not play a role in either case, but the static $M = 0.6$ data show clear evidence of shock-induced separation and stall. The dynamic data at $M = 0.6$ suggest that the formation of shock waves somehow inhibits the development of the vortex-shedding process, although some vestiges of the phenomenon remain. New boundary-layer and flow-field measurements similar to the ones that have been done at lower speeds are needed to resolve this question further.

4.5 Other Types of Motion

Most of the available information concerning dynamic stall has been obtained on airfoils oscillating sinusoidally in pitch about an axis at the quarter-chord. However, limited studies of other forms of periodic and non-periodic motion shown qualitative agreement with most of the results outlined above.

Plunging oscillations, or vertical translational motion, produce an equivalent fluctuating angle of attack, $\alpha_{eff} = -\dot{h}/U_\infty$, superimposed on the mean incidence α_o. Current engineering practice is to assume that the resultant flow fields and airloads are equivalent to those due to pitching oscillations. This appears reasonable for deep stall, as indicated in Fig. 20 (from Ref. 11), but significant differences have been reported for light stall (Refs. 12, 13).

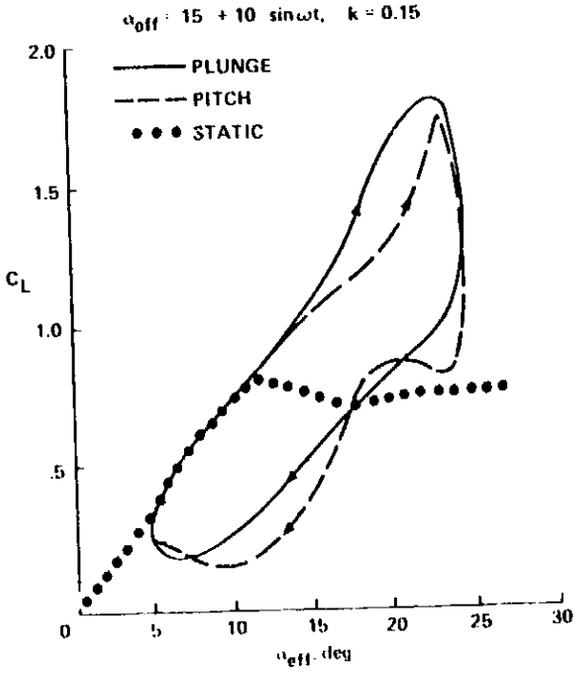

Fig. 20. Comparison of pitch and plunge results in deep stall.

The studies of Maresca et al. (Ref. 11) also established the existence of the vortex-shedding phenomenon and strong hysteresis effects due to translational oscillations in the streamwise direction and at various oblique angles relative to the oncoming flow. In the longitudinal-oscillation case, for example, unsteady effects were found to be strong enough to unstall the airfoil during part of the cycle, even when the incidence was considerably above the static stall angle.

4.6 Three-Dimensional Effects

Despite the fact that almost all practical devices develop three-dimensional flow, common engineering practice is to use so-called strip theory and the two-dimensional stall characteristics outlined above. This is partly due to simplicity and partly due to the acute lack of three-dimensional information.

As a first step, St. Hilaire et al. (Ref. 14) examined the effect of sweeping an oscillating wing model at an angle Λ with respect to the free stream, as shown in Fig. 21. Figure 22 shows typical lift and moment results, respectively, where the coefficients are normalized with respect to the velocity component normal to the leading edge, $U_\infty \cos\Lambda$, and α is similarly defined. Sweep tends to delay the onset of dynamic stall and to reduce the rate of change of C_l and C_M as stall begins. It also reduces somewhat the magnitude of the hysteresis loops.

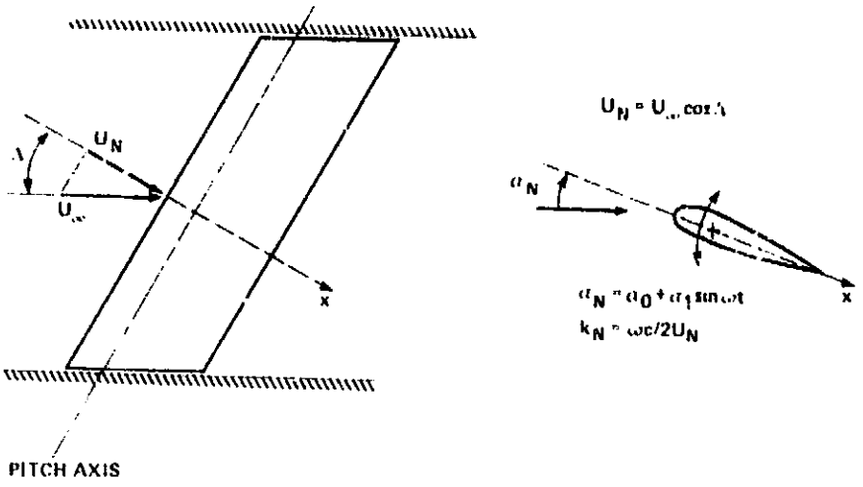

Fig. 21. Sketch of oscillating swept wing experiment.

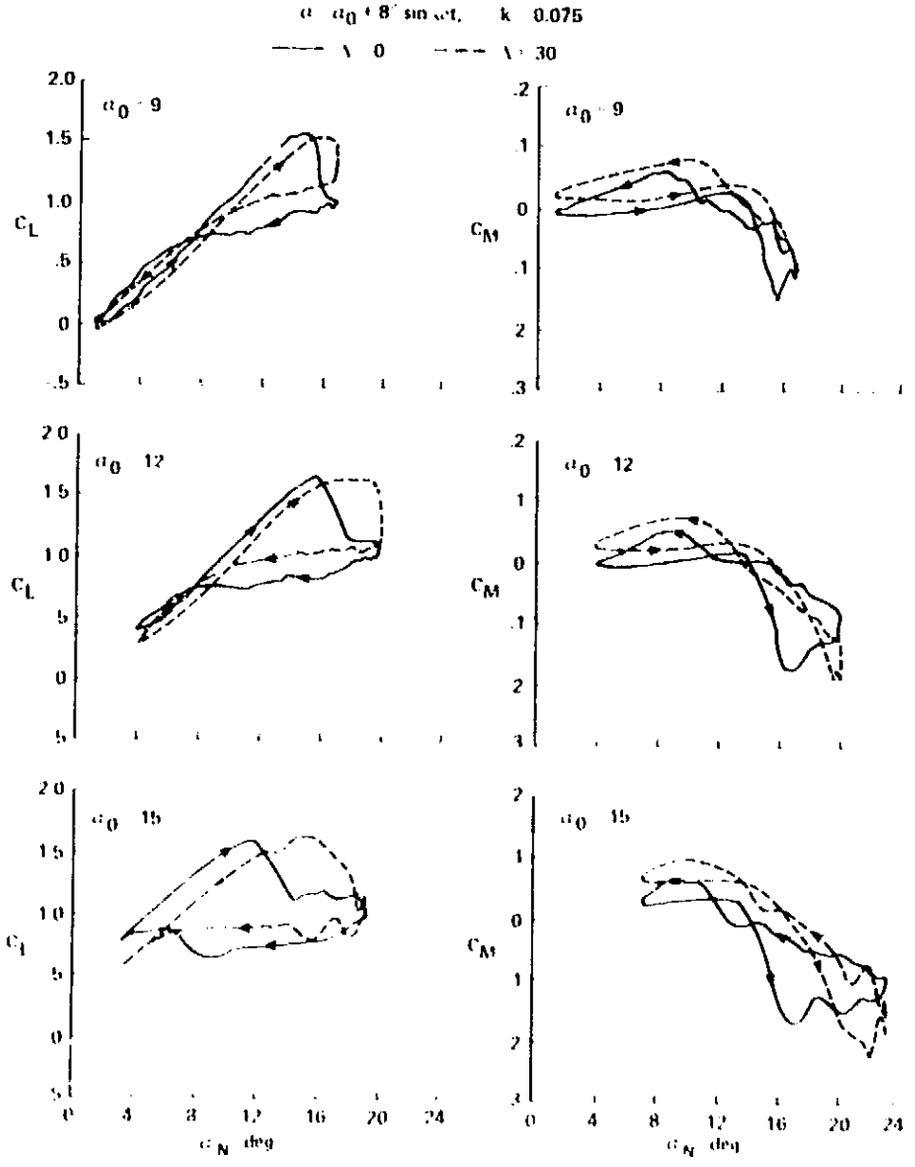

Fig. 22. Effect of sweep on dynamic stall airfoils.

Finally, the measurements of McCroskey and Fisher (Ref. 15) on a model helicopter rotor may be mentioned. At a spanwise station r, the rotor blade element experiences a periodic velocity component $V_N = \Omega r + V_\infty \sin \Omega t$ normal to the leading edge and a spanwise component $V_\infty \cos \Omega t$ due to combined rotational and translational motion of the rotor. In addition, the angle of attack changes periodically due to a complicated combination of pitching and plunging motion.

Figure 23 shows two cases from Ref. 15, where $\Psi = \Omega t$. For the deep stall case, a detailed analysis of the pressure data indicated that the stall events and the airloads were essentially the same as those on an airfoil oscillating in pitch for $90 < \Psi \lesssim 270°$, provided the large-amplitude oscillations in α were approximately matched. The vortex-shedding phenomenon appeared at $\Psi \approx 210°$, followed by large transient overshoots in C_L and C_M that excited stall flutter at the torsional natural frequency of the blades.

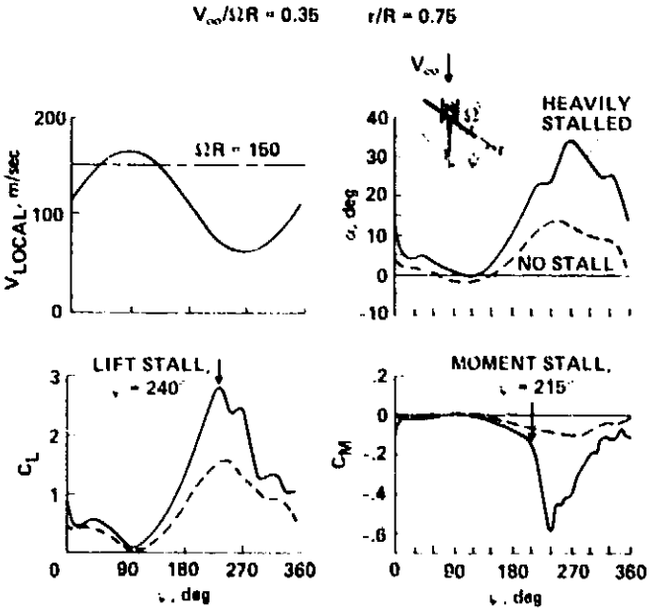

Fig. 23. Blade element environment and airloads on a model rotor.

However, these and other model rotor data indicate that three-dimensional effects produce significantly larger lift for $270° < \Psi < 360$, after the vortex passes off the blade and into the wake. At the moment, therefore, the use of two-dimensional airfoil data to predict the airloads on devices such as helicopter rotors and wind turbines should be viewed with a certain amount of caution.

5. METHODS OF CALCULATION

The physical aspects of the phenomenon of dynamic stall have been outlined in previous sections. We consider now a number of special techniques that have been suggested for predicting the engineering quantities of interest, such as the instantaneous values of lift, drag, and pitching moment. It should be emphasized that all of these methods are still being developed, refined, and improved, even in two spatial dimensions. Furthermore, all of the techniques invoke some sort of simplifying assumptions and approximations and are tailored to the specific features of some particular stall regime or to a relatively narrow range of parameters.

5.1 Discrete Potential Vortex Approach

A promising analytical approach to the deep dynamic stall regime in incompressible flow takes its cue from the discrete vortex model that has been applied to bluff-body separation, sketched in Fig. 24(a). In the simpler case of a circular cylinder in the low subcritical Reynolds number regime, alternate or staggered rows of potential vortices produce the essential features of the forces on the cylinder, but the vortex spacing and frequency have to be specified empirically.

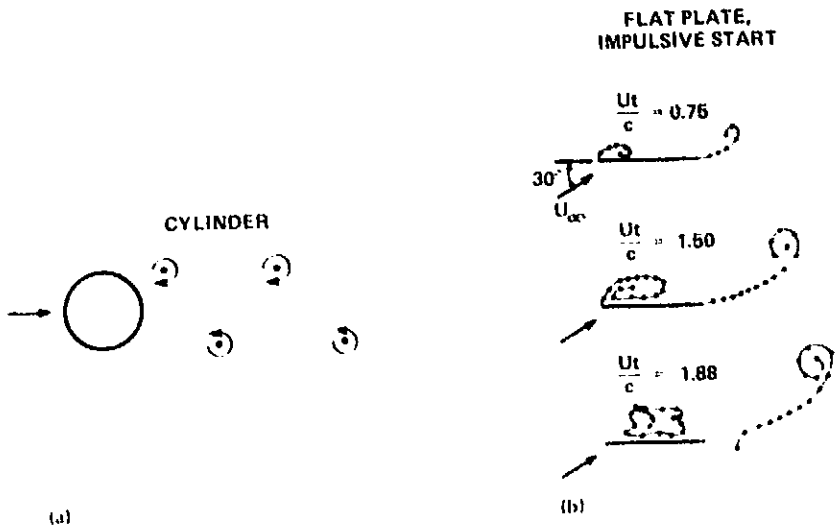

Fig. 24. The discrete vortex model.

The vortex-shedding phenomenon on a thin flat plate was first modeled by a series of emitted vortices by Ham (Ref. 16), as shown on the right in Fig. 24. Each vortex moves under the influence of all the others, and the result is a tendency for the individual filaments to coalesce into a structure that resembles the experimentally observed features of dynamic stall.

As in the case of the cylinder, assumptions must be made regarding the geometry and strength of the vortex emissions. In fact, the crux of this general approach lies in choosing the strength assigned to each vortex and in the mechanism for relating the birth of the vortices to the boundary-layer-separation characteristics on the body. Ham started the process at an arbitrarily assumed incidence and adjusted the strength of the vortex emissions to ensure stagnation points at the two edges of the plate. This amounts to imposing a special Kutta condition at the leading edge as well as at the trailing edge.

This approach has been extended by Baudu et al. (Ref. 17) for an airfoil with finite thickness and combined with a boundary-layer analysis to provide a definition of the separation point on the upper surface. The vortices are emitted from the point of boundary-layer separation in the leading-edge region, and the circulation of the vortex filaments grows according to the flux of vorticity from the boundary layer. The flow field resulting from the combination of the body and the free vortices is calculated by an adaptation of the numerical potential-flow technique of Giesing (Ref. 18).

Further refinements and extensions of the discrete vortex approach have been made by Ono et al. (Ref. 19). Unlike previous analyses, the airfoil boundary layer is approximated by a layer of discrete vortices whose strengths

are chosen to satisfy the no-slip condition on the surface. The surface vortex layer is divided into a small number of finite-length elements, with one vortex filament just off the surface for each element, as shown schematically in Fig. 25. At time step N, the vortex $\gamma^{N,k}$ induces a surface velocity $\Delta q^{N,k} = [\phi^{N,k+1} - \phi^{N,k}]/[s^{k+1} - s^{k}]$ that cancels the velocity that would otherwise exist for irrotational flow around the body. Each vortex filament is then allowed to convect to a new position at the next time step under the influence of the flow field due to the body and all of the vortices. As time progresses and new vortices are created near the body, "separation" and the clustering of vortices into something resembling the vortex-shedding phenomenon observed in experiments evolves naturally. Figure 26 shows a typical pattern of vortices and the resultant streamlines.

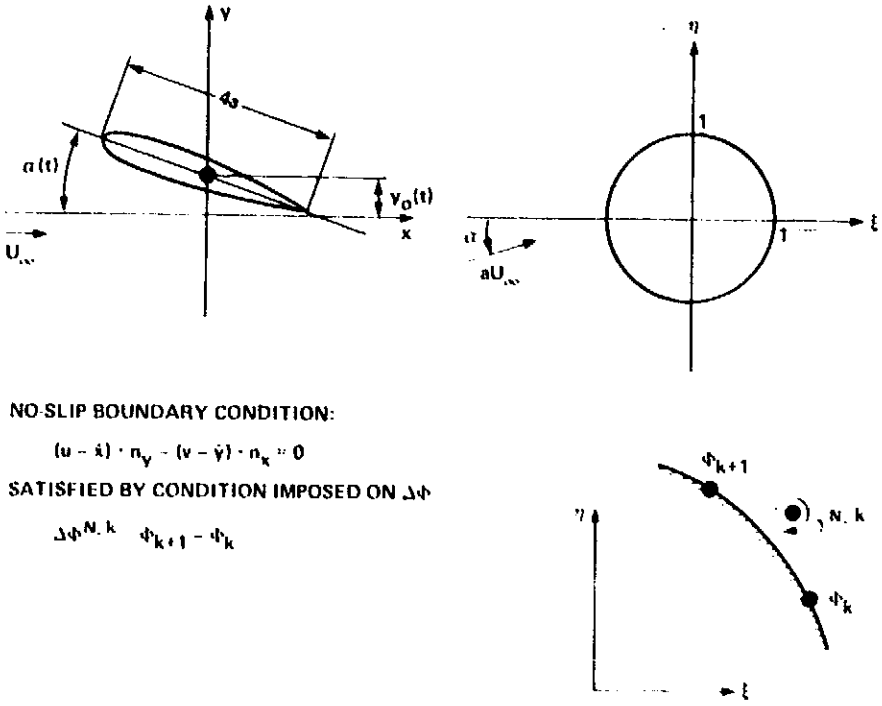

Fig. 26. Application of the discrete vortex model to an oscillating airfoil.

In principle, the only free parameters in this method are the size of the time steps and the number of elements used to represent the boundary layer around the body. However, since the number of generated vortices continually increases, computational limitations dictated two further approximations in the calculations that have been performed to date (Ref. 19). The first was to allow clusters of vortices far away from the body to be replaced by a single equivalent vortex. Second, the number of elements representing the boundary layer was severely limited after the first time step. The results so obtained appear qualitatively correct for dynamic stall at low Reynolds numbers, but the method needs further development to become a practical engineering tool.

5.2 Zonal Methods

Especially in the light stall regime, the viscous region tends to remain relatively thin. For flow fields of this type (Fig. 27), the various regions can be modeled separately and coupled in some appropriate fashion.

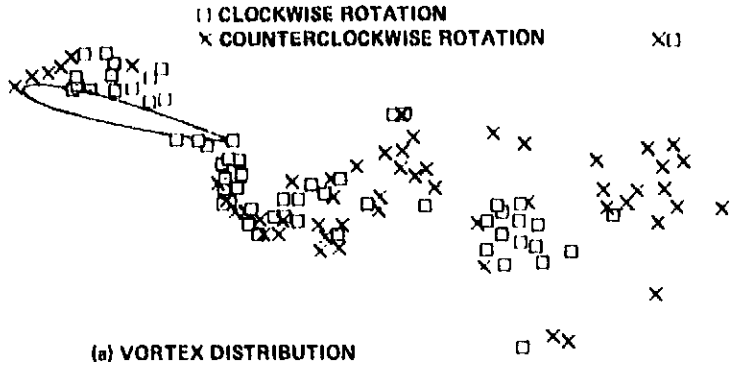

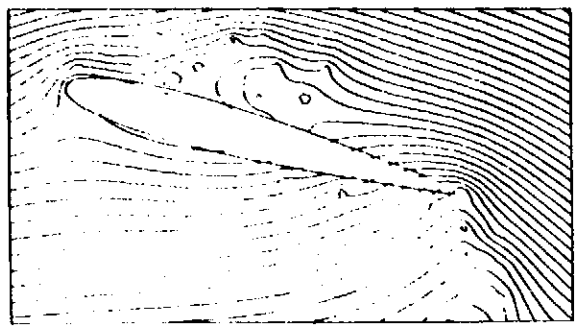

Fig. 26. Discrete vortex results for an oscillating airfoil; $\alpha = 15° + 15° \sin \omega t$, $k = 2.45$.

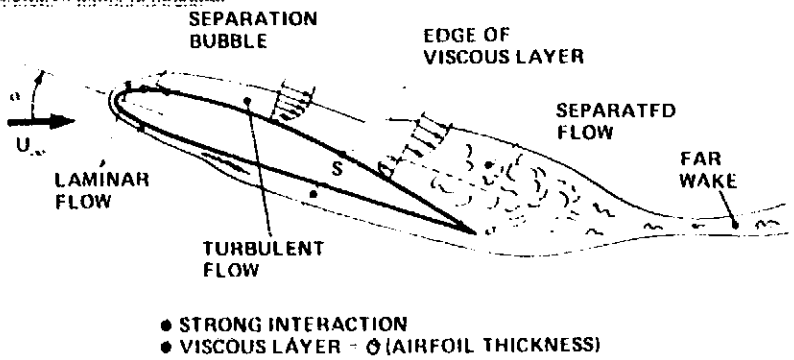

Fig. 27. Sketch of the flow field for light dynamic stall with trailing edge separation.

5.2.1 Thin-boundary-layer approach- The classical Prandtl boundary-layer equations, incorporating some sort of turbulence modeling and modified to include unsteady terms, have been used by several authors (see Ref. 1) to investigate some of the characteristics of dynamic stall. These studies have shed light on the delay in the onset of dynamic stall and on the differences between steady and unsteady separation; but lacking any coupling between the viscous and inviscid regions, this approach has very limited quantitative usefulness. Also, it gives few clues to the mechanisms responsible for the vortex-shedding phenomenon, which is such a prominent feature of dynamic stall.

5.2.2 Coupled viscous-inviscid interactions- The analysis of Crimi and Reeves (Ref. 20) retained boundary-layer concepts wherever possible, while allowing a strong coupling to exist between the viscous flow in the separated

zone and the surrounding inviscid flow. These authors modeled the inviscid flow with an extension of unsteady thin-airfoil theory, representing the airfoil and the separated flow with distributed source and vortex singularities. Finite-difference calculations of the unsteady boundary-layer equations were performed for the attached flow, using an eddy-viscosity model for the turbulent flow. In the absence of boundary-layer separation, no interaction between the viscous and inviscid flow was considered. The leading-edge separation bubble formation was analyzed to determine whether reattachment would occur or whether the bubble would "burst," and this criterion was used to distinguish between leading-edge and trailing-edge stall.

A number of approximations and assumptions were made in developing the analysis, but most of the essential flow elements seem to have been included. Although the application to trailing-edge stall was not attempted, the method was applied to a variety of unsteady airfoil and helicopter problems, with varying degrees of success. One of the main faults was that the basic prediction of whether the leading-edge bubble would burst did not seem to depend on Reynolds number and leading-edge geometry in the proper manner. Attempts by the present author to apply the method to the prediction of the static and dynamic stall characteristics of several helicopter-type airfoils which are thought to stall by the bubble bursting mechanism did not correlate well with experiments. Furthermore, the viscous part of the analysis does not account for the feature of a thin layer of reversed flow near the wall before and during the beginning of trailing-edge stall, nor for highly organized vortex-shedding, as discussed earlier.

More recently, Rao et al. (Ref. 21) extended a steady viscous-inviscid interaction method (Ref. 22) to dynamic stall by introducing an empirical delay parameter, $\Delta\tau$, into an effective angle of attack, $\alpha_{eff} = \alpha_0 + \alpha_1 \sin(\omega t - \omega\Delta\tau)$. The parameter $\Delta\tau$ is considered to be a function of α_1 and k for a given airfoil and is constant throughout the cycle. The potential flow at each value of α_{eff} is calculated by panel methods, with a distribution of sources and vortices representing the airfoil and vortex sheets representing free-shear layers. The free-shear layers approximately coincide with the edges of the viscous layers in Fig. 27 and are slip-surface streamlines. They define an effective wake, which is assumed to be irrotational and to have a constant total pressure less than that of the free stream. The point where the upper-surface vortex sheet leaves the airfoil is determined by an integral boundary-layer calculation of the separation point (point S in Fig. 27). The resultant configuration is sketched in Fig. 28. Iterations are performed at each value of α_{eff} until the wake shape and separation points converge; actually, the convergence criterion is that C_L change less than 1%.

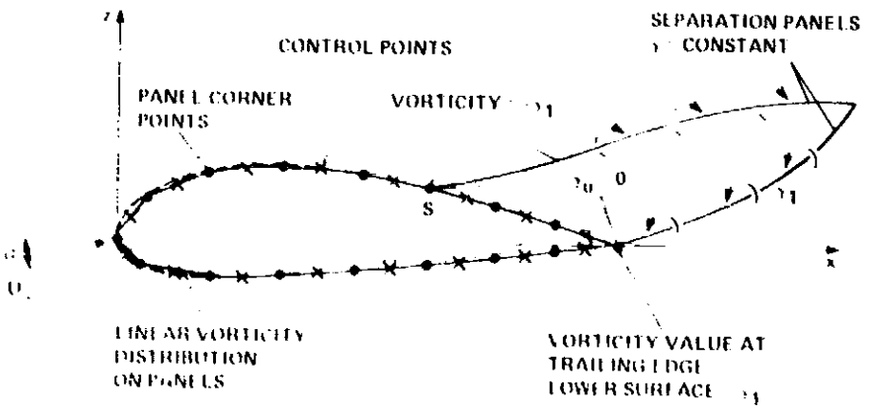

Fig. 28. [illegible] separated flow model for unsteady [illegible].

Although realistic hysteresis loops of C_L and C_M versus α have been calculated, the results published so far (Ref. 21) cannot be considered predictive because they depend heavily on the arbitrary choice of $\Delta\tau$. And as in the analysis of Crimi and Reeves (Ref. 20), neither the special features of unsteady reversed flow nor strong vortex shedding have been included. However, with additional modifications and refinements, these zonal methods could offer a reasonable balance of rigor, accuracy, and computational efficiency, at least for light dynamic stall.

5.3 Navier-Stokes Calculations

The limitations and approximations of zonal methods and the questions of unsteady separation models can, in principle, be avoided by solving the full Navier-Stokes equations. However, turbulence must be modeled and a number of computational difficulties must be overcome if this approach is to be realistic for most practical applications.

Several recently developed methods for laminar flows, discussed in Refs. 1 to 4, have shed considerable light on the physical mechanisms of deep dynamic stall at low Reynolds numbers and have laid the computational foundations for high-Reynolds-number solutions of the so-called Reynolds-averaged, Navier-Stokes equations. For incompressible flow in two dimensions, they may be expressed as:

$$\nabla\cdot\bar{q} = 0 \tag{1}$$

$$\frac{\partial\bar{q}}{\partial t} + \bar{q}\cdot\nabla\bar{q} = -\frac{1}{\rho}\nabla p + \nu\nabla^2\bar{q} - \frac{\partial\overline{u_i u_j}}{\partial x_j} \tag{2}$$

where $\bar{q}$ represents the velocity vector (u,v) time-averaged over an interval short with respect to the time scale of the motion, but long with respect to the time scale of the turbulence, and $-\rho\overline{u_i u_j}$ is the Reynolds stress due to the random turbulent fluctuations. The Reynolds stress term vanishes in laminar flow and is to be modeled (empirically or otherwise) in the turbulent case. The particular representation of the detailed physics of turbulence is crucial in many steady-flow problems that are dominated by viscous effects. However, the importance of turbulence modeling in dynamic stall has yet to be established.

Numerical codes using various turbulence models that have been developed for steady flow are currently under development at several research centers. A few very preliminary results have been published (Refs. 23, 24) and more will become available in the near future. However, quite apart from the question of the large computational times and storages required, it will be some time before these codes are adequately tested and verified. Nevertheless, the careful and selective analysis of new numerical results for both light and deep dynamic stall will be especially beneficial in guiding the development of more approximate engineering analyses and prediction methods based on empirical correlations of wind-tunnel data.

5.4 Empirical Correlation Techniques

The helicopter industry has developed several engineering prediction techniques based on empirical correlations of wind-tunnel data for estimating the unsteady airloads on oscillating airfoils. These methods seek to correlate force and moment data obtained from relatively simple wind-tunnel tests in formulations that show the effects of the numerous relevant parameters

such as airfoil shape, Mach number, amplitude and frequency of oscillations, mean angle, and type of motion.

Common to all the available literature relevant to dynamic stall is the observation that unsteady effects increase with increasing pitch rate, that is, rate of change of airfoil incidence. It is also evident that the dynamic stall events require finite times to develop. Therefore, some form of the dimensionless parameters $\dot{\alpha}c/U_\infty$ and $U_\infty \Delta t/c$ appears in all of the empirical methods. Another common aspect is that the empirical correlations are used as corrections to steady airfoil data, so that most geometrical, Reynolds number, and Mach number effects are only accounted for insofar as they determine the static section characteristics.

The highlights of several methods currently in use by the helicopter industry are outlined below. More detailed accounts of each can be found in the references cited and in Refs. 2 to 4.

5.4.1 Boeing-Vertol gamma function method (Refs. 25, 26)- The onset of dynamic stall is assumed to occur at $\alpha_{DS} = \alpha_{SS} + \Delta\alpha_D$, where α_{SS} is the static stall angle and $\Delta\alpha_D = \gamma\sqrt{\dot{\alpha}c/U_\infty}$. The quantity γ, which is the essential empirical function, depends on airfoil geometry and Mach number and is different for lift and moment stall. The gamma functions were generated from a large amount of data generated in a transonic wind-tunnel test of various airfoils oscillating sinusoidally in pitch. The force and moment coefficients are constructed from static data using an equivalent angle of attack that accounts for unsteady potential-flow effects, α_{eq}, and a reference angle, $\alpha_r = \alpha \pm \gamma\sqrt{|\dot{\alpha}c/U_\infty|}$,* as follows:

$$\left.\begin{aligned} C_L &= [\alpha_{eq}/\alpha_r]C_L(\alpha_r) \\ C_D &= C_D(\alpha_r) \end{aligned}\right\} \alpha_r \text{ based on } \gamma_{lift}$$
$$C_M = [0.25 - X_{cp}]C_L \qquad (3)$$

The location of the aerodynamic center of pressure, X_{cp}, is specified empirically in the current version of the method. This formulation permits a dynamic overshoot of C_L above its maximum static value, but not of C_D. Also, note that α_{DS} is always less than α_{max}, since $\Delta\alpha_D = 0$ when $\dot{\alpha} = 0$.

5.4.2 UTRC α, A, B method (Refs. 27, 28)- A table-lookup correlation method, which has recently been synthesized into a more streamlined format, was developed at United Technologies Research Center to determine C_L and C_M from three independent parameters of the airfoil motion. The choice of the parameters was inspired by thin-airfoil potential theory; they are instantaneous incidence $\alpha(t)$, angular velocity parameter $A = \dot{\alpha}c/2U_\infty$, and angular acceleration parameter $B = \ddot{\alpha}c^2/4U_\infty^2$. It is interesting to note that these three parameters are sufficient to define to engineering accuracy the matching $\alpha(t)$ histories for the two cases shown in Fig. 17. The data base for the empirical correlations came from experiments on an NACA 0012 airfoil oscillating in pitch at $M \leq 0.3$, including both sinusoidal and nonsinusoidal motion. None of the data attained the extreme values that have been observed to accompany the fully developed vortex-shedding phenomenon of deep stall.

5.4.3 MIT method (Ref. 29)- This method is basically an empirical representation of the forces and moments due to the vortex-shedding phenomenon for ramp changes in angle of attack. The actual angle of dynamic stall must be

*The sign of the radical term is taken to be opposite to the sign of $\dot{\alpha}$.

specified separately; the value $\alpha_{DS} = \alpha_{SS} + 3°$ has normally been used. For $\alpha_{SS} < \alpha < \alpha_{DS}$, the data are extrapolated from below static stall. Starting at $\alpha = \alpha_{DS}$, C_L and C_M are assumed to increase linearly with time over a specified time interval, from inviscid values to peak values that depend on $\dot{\alpha}c/U_\infty$ at the instant of dynamic stall. If this is attained before $\alpha = \alpha_{max}$, then C_L and C_M remain constant until α_{max}. They decay exponentially* with preassigned time constants thereafter until the static stall values are attained. These new values are retained until $\alpha = \alpha_{SS}$ on the downstroke, when the unstalled static section characteristics are reattained.

5.4.4 Lockheed method (Refs. 30, 31)- This combined analytical and empirical modeling of dynamic stall incorporates phase-lag time constants and pitch-rate-dependent, stall-angle delay increments into a ficticious effective angle of attack. This effective angle is used to construct C_L and C_M from static airfoil characteristics and a linear combination of a number of separate dynamic stall elements. Some of these elements are assumed to be analogous to flow phenomena that have been treated elsewhere in the literature, such as leading-edge jets, the lag in circulation buildup on a pitching airfoil in potential flow, separation over moving walls, fluctuating pressure propagation in turbulent boundary layers, and the vortex lift due to leading-edge vortices on delta wings. Other elements are modeled directly from dynamic stall measurements on oscillating airfoils. In this sense, the method has more degrees of freedom than any of the others, and information from many sources has been utilized.

At low frequency, the phase lag of the effective incidence is linearly proportional to k. The latest version (Ref. 31) includes increments of C_L and C_M due to the vortex-shedding phenomenon that are proportional to $\sin^2 \alpha$. Compressibility corrections are developed from various applications of the Prandtl-Glauert rule. This is the only method which distinguishes between pitching and plunging motion.

5.4.5 Time-delay methods (Refs. 4, 32)- The basic idea of this approach is that each dynamic stall event is governed by a separate universal dimensionless time constant of the form $\tau = U_\infty \Delta t/c$, regardless of the time history of the motion; τ may be identified with the parameter $s = 2U_\infty t/c$, which is fundamental to expressions for the indicial aerodynamic response in the attached-flow regime. The construction of the force and moment characteristics can be explained with the aid of Fig. 29. If t_o is the time at which the angle of attack passes through α_{SS}, then moment stall begins at time $t_1 = t_o + \tau_1 c/U_\infty$ and C_{Lmax} occurs at $t_2 = t_o + \tau_2 c/U_\infty$. For $t < t_1$ (line segments 1 in the figure), the values of C_L and C_M are taken from unsteady potential theory. For $t_1 < t < t_2$, C_L continues this trend, but the aerodynamic center of pressure moves rearward along the locus of the static curve of X_{cp} versus α. Therefore, $-C_M$ increases along line segment 2 according to the relation $C_M = (0.25 - X_{cp})C_L$ during this time interval.

After lift stall at $t = t_2$, C_L decreases by an empirical exponential law with respect to time, whereas C_M is calculated from the same relation as before. Line segments 3 terminate at $\alpha = \alpha_{SS}$ and at a value of C_L that corresponds to a fully separated approximation, indicated in Fig. 29. The return to minimum incidence, line segments 4, is governed by still other exponential functions.

The Sikorsky version (Ref. 32) now uses the values $\tau_1 = 2.5$ and $\tau_2 = 5.0$ for the time constants. It makes no provision for compressibility phenomena other than in the static characteristics for $C_L(\alpha)$ and $X_{cp}(\alpha)$, nor

*A linear decay over a time interval $\Delta\omega t = 0.2$ has also been used.

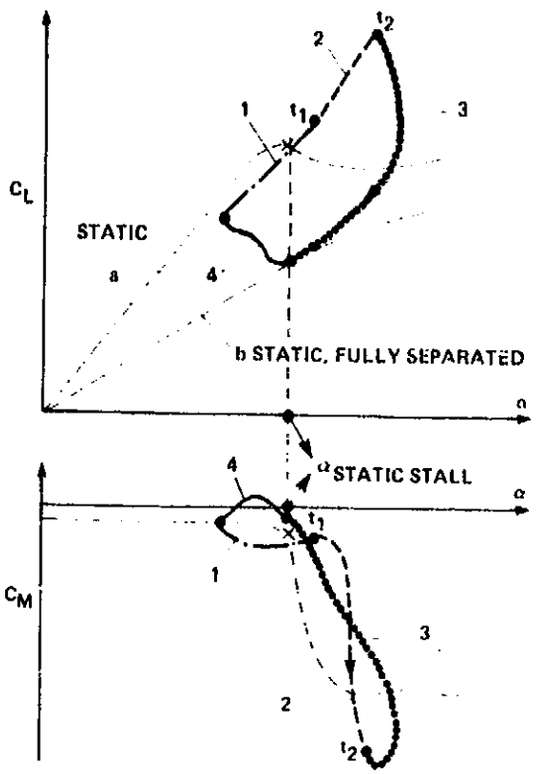

Fig. 29. Sketch of the time-delay method.

for the contribution of the vortex-shedding phenomenon to C_L and C_M. The Westlands version (Ref. 4) includes a dynamic leading-edge stall criterion in τ_1 that partially accounts for compressibility effects and changeovers from trailing-edge to leading-edge stall. This method also seems to be the only one to recognize the simple drag relationship, $C_D \cong C_L \tan \alpha$, that obtains once the leading-edge suction is lost at τ_1.

5.4.6 ONERA method (Ref. 33)- In contrast to the preceding methods that essentially curve-fit experimental data with various algebraic or transcendental functions, this recent method utilizes a system of ordinary differential equations. If F represents a dynamic force coefficient, e.g., C_L or C_M, and F_o represents the corresponding static coefficient, then F is split into a "linear" part F_1 and a "nonlinear" part F_2; the system is written as

$$F = F_1 + F_2 \tag{4}$$

$$\dot{F}_1 + a_1 F_1 = a_1 F_{1in} + a_2 \dot{\alpha} + a_3 \ddot{\alpha} \tag{5}$$

$$\ddot{F}_2 + a_4 \dot{F}_2 + a_5 F_2 = -a_5 \Delta F_o + a_6 \dot{\alpha} \frac{d\Delta F_o}{d\alpha} \tag{6}$$

Here ΔF_o represents the departure of the *static* coefficient from its linear trend, as illustrated for lift in Fig. 30, t is dimensionless time, and $a_1, a_2, \ldots, a_5$ are coefficients to be determined empirically.

For illustrative purposes, sinusoidal pitch oscillations, $\alpha = \alpha_o + \alpha_1 \sin \omega t$, are considered. Below stall, that is, $\alpha_{max} < \alpha_{ss}$, $F_2 = 0$ and Eq. (5) with constant coefficients closely approximates the behavior of unsteady, linear, thin-airfoil theory. In the stall domain, however, a_n varies as a function of α and hence with time. Each a_n is evaluated by local linearization about α_o. That is, data from a series of small-amplitude oscillations about various values of α_o are used to develop empirical relations for $a_n(\alpha_o)$. This requires a large quantity of small-amplitude data, but ONERA has developed a systematic way of generating these data very efficiently, once the peculiar requirements of the method are recognized.

Figure 31 derived from Ref. 33 illustrates some predictions for moderate-amplitude oscillations using the a_n's derived from data for which $\alpha_1 = 1°$ or less. Comparable results were obtained for C_M.

5.4.7 Discussion of the methods- All the methods described above provide estimates of the effects of unsteady incidence changes, but each has some shortcomings. Each method manages to reproduce reasonably well most of the data sets that were used in its development, but almost no comparisons have been made between any given method and independent sets of data.

One notable exception has been described in Refs. 2 to 4. With the assistance of the originators and their colleagues, the present writer was able to compare the results of several of the aforementioned methods to an independent deep stall experiment. Four predicted quantities were compared: the phase angle, ωt, at the onset of moment stall; the phase angle and maximum value of the normal force coefficient; and the value of $C_{M_{min}}$.

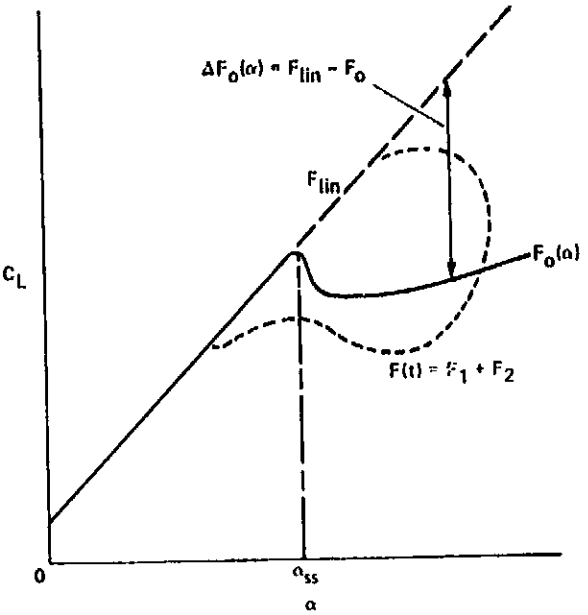

Fig. 30. Sketch of the components of the ONERA method.

The Boeing-Vertol and UTRC methods tended to underpredict the effect of the dynamic stall vortex on maximum force and moment from the experiment, especially for large α_1, whereas the MIT and Lockheed methods overemphasized the importance of vortex shedding on C_M. The Sikorsky time-delay method gave reasonable values for $C_{L_{max}}$ and $C_{M_{min}}$. However, this was somewhat fortuitous because it tended to predict lift stall later than the experiment, thereby compensating for the failure to include the extra lift due to the vortex. The phase-angle results for the other methods were mixed.

A preliminary examination of the newer ONERA method has been encouraging, but it has also revealed that it is not well suited to data sets that were generated without regard to its small-amplitude and high-frequency requirements.

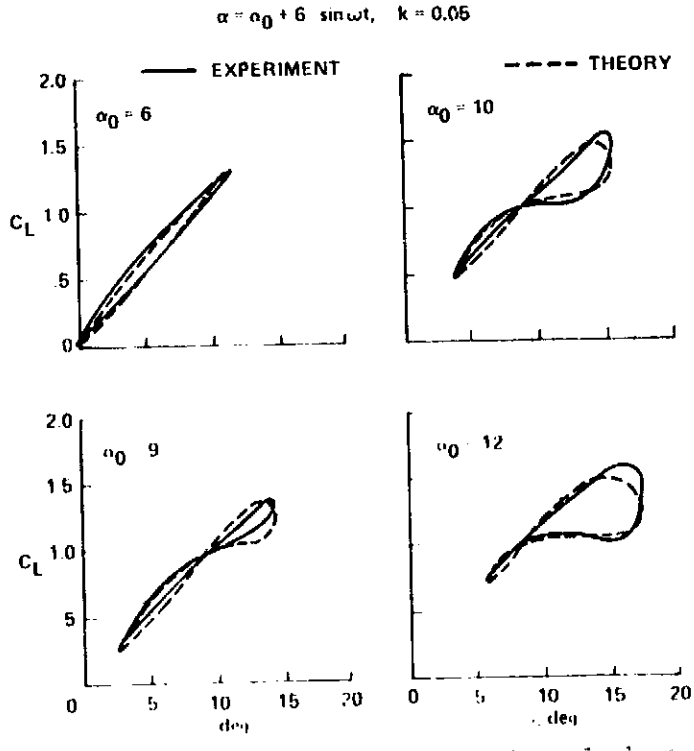

Fig. 31. [illegible] prediction by the ONERA method at $M_\infty = 0.3$.

Reasonable predictions of surprisingly large-amplitude results were obtained at low reduced frequencies, but not when both α_1 and k were relatively large, e.g., $\alpha_1 = 10°$ and $k = 0.10$. Also, it does not appear to be able to model changes in stall behavior, such as, for example, static trailing-edge converting to dynamic leading-edge stall.

6. CONCLUDING REMARKS

The general features of dynamic stall on oscillating airfoils have been explained in terms of the vortex-shedding phenomenon, and the important differences between static stall, light dynamic stall, and deep stall have been described. The present level of knowledge has been enhanced somewhat by potential theory, boundary-layer theory, and Navier-Stokes calculations. However, most of what we know today has come from experiments and semiempirical modeling of the fluid dynamic forces and moments. The prediction techniques that have been developed for helicopter applications are considerably better than what was available a few years ago, but more satisfactory results await a better theoretical understanding of the effects of various types of airfoil motion and three-dimensional effects.

The calculation of the flow around an oscillating airfoil at high incidence is a formidable task. The qualitative features of dynamic stall airloads are captured by the empirical prediction methods, but all of them need further quantitative improvements. At the present time, they are used for engineering purposes in preference to the analytical and numerical techniques that were described. However, this is likely to change, especially for the light stall domain, as the current efforts to develop analytical tools for two-dimensional flows begin to mature. Experiments, theoretical modeling, and numerical analyses can all be expected to play major roles in assessing and predicting the three-dimensional effects encountered in practice, but which are poorly understood at the present time.

REFERENCES

1. McCroskey, W. J.: "Some Current Research in Unsteady Fluid Dynamics — the 1976 Freeman Scholar Lecture." ASME J. Fluids Engineering, vol. 99, no. 1, 1977, pp. 8-39.

2. McCroskey, W. J.: "Some Separation Problems for Slender Bodies," and "Prediction of Unsteady Separated Flows on Oscillating Airfoils." Papers no. 8 and 12, AGARD Lecture Series no. 94, 1978.

3. Philippe, J. J.: "Le Déchrochage Dynamique: un Exemple d'Interaction Forte entre Ecoulements Visqueux et Nonvisqueux," Paper no. 21, AGARD CP-227, 1977.

4. Beddoes, T. S.: "A Qualitative Discussion of Dynamic Stall," and "Prediction Methods for Unsteady Separated Flows," Papers no. 3 and 15, AGARD R-679, 1980.

5. Young, W. H., Jr.: "Fluid Mechanics Mechanisms in the Stall Process of Airfoils for Helicopters," Symposium on Numerical and Physical Aspects of Aerodynamic Flows," Long Beach, California, 1981.

6. McAlister, K. W.; and Carr, L. W.: "Water-Tunnel Experiments on an Oscillating Airfoil at Re = 21000," NASA TM-78446, 1978.

7. McCroskey, W. J.; Carr, L. W.; and McAlister, K. W.: "Dynamic Stall Experiments on Oscillating Airfoils," J. AIAA, vol. 14, no. 1, 1976, pp. 57-63.

8. McCroskey, W. J., et al.: "Dynamic Stall on Advanced Airfoil Sections," American Helicopter Society Preprint 80-01, 1980.

9. McCroskey, W. J.; Pucci, S. L.: "Viscous-Inviscid Interaction on Oscillating Airfoils in Subsonic Flow," AIAA Paper 81-0051, 1981.

10. Liiva, J.: "Unsteady Aerodynamics and Stall Effects on Helicopter Rotor Blade Sections." J. Aircraft, vol. 6, no. 1, 1969, pp. 46-51.

11. Maresca, C.; Favier, D.; and Rebont, J.: "Unsteady Aerodynamics of an Airfoil at High Angle of Incidence Performing Various Linear Oscillations in a Uniform Stream." Paper no. 12, Fifth European Rotorcraft and Powered Lift Aircraft Forum, Amsterdam, Netherlands, 1979.

12. Fukushima, T.; and Dadone, L. U.: "Comparison of Dynamic Stall Phenomena for Pitching and Vertical Translation Motions." NASA CR-2793, 1977.

13. Carta, F. O.: "A Comparison of the Pitching and Plunging Response of an Oscillating Airfoil." NASA CR-3172, 1979.

14. St. Hilaire, A. O.; Carta, F. O.; and Jepson, W. D.: The Influence of Sweep on the Aerodynamic Loading of an Oscillating NACA 0012 Airfoil." AHS Preprint 79-4, 1979.

15. McCroskey, W. J.; and Fisher, R. K., Jr.: "Detailed Aerodynamic Measurements on a Model Rotor in the Blade-Stall Regime." J. AHS, vol. 17, no. 1, 1972, pp. 20-30.

16. Ham, N. D.: "Aerodynamic Loading on a Two-Dimensional Airfoil during Dynamic Stall." J. AIAA, vol. 6, no. 10, 1968, pp. 1927-1934.

17. Baudu, N.; Sagner, M.; and Souquet, J.: "Modelisation du Déchrochage Dynamique d'un Profil Oscillant." AAAF 10th Colloque d'Aéronautique Appliquée, Lille, France, 1973.

18. Giesing, J. P.: "Nonlinear Two-Dimensional Potential Flow with Lift." J. Aircraft, vol. 5, no. 2, 1968, pp. 135-143.

19. Ono, K.; Kuwahara, K.; and Oshima, K.: "Numerical Analysis of Dynamic Stall Phenomena of an Oscillating Airfoil by the Discrete Vortex Approximation." Paper no. 8, Seventh International Conference on Numerical Methods in Fluid Dynamics, Stanford, California, 1980.

20. Crimi, P.; and Reeves, B. L.: "A Method for Analyzing Dynamic Stall of Helicopter Rotor Blades." NASA CR-2009, 1972; also NASA CR-2335, 1974.

21. Rao, B. M.; Maskew, B.; and Dvorak, F. A.: "Theoretical Prediction of Dynamic Stall on Oscillating Airfoils," AHS Paper 78-62, 1978.

22. Maskew, B.; and Dvorak, F. A.: "Investigation of Separation Models for the Prediction of $C_{l_{max}}$." J. AHS, vol 23, no. 2, 1978, pp. 2-8.

23. Shamroth, S. J.; and Gibeling, H. J.: "The Prediction of the Turbulent Flow Field about an Isolated Airfoil." AIAA Paper 79-1543, 1979; also NASA CR-3183, 1979.

24. Sugavanum, A.; and Wu, J. C.: "Numerical Study of Separated Turbulent Flow over Airfoils." AIAA Paper 80-1441, 1980.

25. Harris, F. D.; Tarzanin, F. J., Jr.; and Fisher, R. K., Jr.: "Rotor High-Speed Performance; Theory vs Test." J. AHS, vol. 15, no. 3, 1970, pp. 35-44.

26. Cormont, R. E.: "A Mathematical Model of Unsteady Aerodynamics and Radial Flow for Application to Helicopter Rotors." U.S. Army AMRDL-Eustis Directorate Report TR-72-67, 1973.

27. Carta, F. O. et al.: "Investigation of Airfoil Dynamic Stall and Its Influence on Helicopter Control Loads." U.S. Army AMRDL-Eustis Directorate Report TR-72-51, 1972.

28. Bielawa, R. L.: "Synthesized Unsteady Airfoil Data with Applications to Stall-Flutter Calculations." AHS Preprint no. 935, 1975.

29. Johnson, W.: "The Effect of Dynamic Stall on the Response and Airloading of Helicopter Rotor Blades." J. AHS, vol. 14, no. 2, 1969, pp. 68-79.

30. Ericsson, L. E.; and Reding, J. P.: "Dynamic Stall Analysis in the Light of Recent Numerical and Experimental Results." J. Aircraft, vol. 13, no. 4, 1976, pp. 248-255.

31. Ericsson, L. E.; and Reding, J. P.: "Dynamic Stall at High Frequency and Large Amplitude." J. Aircraft, vol. 17, no. 3, 1980, pp. 136-142.

32. Carlson, R. G. et al.: "Dynamic Stall Modeling and Correlation with Experimental Data on Airfoils and Rotors." Paper no. 2, NASA SP-352, 1974.

33. Tran, C. T.; and Petot, D.: "Semi-Empirical Model for the Dynamic Stall of Airfoils in View of the Application to the Calculation of Responses of a Helicopter Blade in Forward Flight." Paper no. 48, Sixth European Rotorcraft and Powered-Lift Aircraft Forum, Bristol, England, 1980.